© 2024. Published by The Company of Biologists Ltd | Journal of Cell Science (2024) 137, jcs262281. doi:10.1242/jcs.262281

TOOLS AND RESOURCES

SPECIAL ISSUE
IMAGING CELL ARCHITECTURE AND DYNAMICS

Myosin II tension sensors visualize force generation within the actin cytoskeleton in living cells

Ryan G. Hart[1,2], Divya Kota[3], Fangjia Li[4], Mengdi Zhang[4], Diego Ramallo[5], Andrew J. Price[5], Karla L. Otterpohl[1], Steve J. Smith[3], Alexander R. Dunn[6], Mark O. Huising[2,7], Jing Liu[4,8,*] and Indra Chandrasekar[1,9,*]

ABSTRACT

Nonmuscle myosin II (NMII) generates cytoskeletal forces that drive cell division, embryogenesis, muscle contraction and many other cellular functions. However, at present there is no method that can directly measure the forces generated by myosins in living cells. Here, we describe a Förster resonance energy transfer (FRET)-based tension sensor that can detect myosin-associated force along the filamentous actin network. Fluorescence lifetime imaging microscopy (FLIM)-FRET measurements indicate that the forces generated by NMII isoform B (NMIIB) exhibit significant spatial and temporal heterogeneity as a function of donor lifetime and fluorophore energy exchange. These measurements provide a proxy for inferred forces that vary widely along the actin cytoskeleton. This initial report highlights the potential utility of myosin-based tension sensors in elucidating the roles of cytoskeletal contractility in a wide variety of contexts.

KEY WORDS: Actomyosin, Force, Tension sensor, Fluorescence lifetime imaging microscopy, FLIM, Actin dynamics, Live-cell imaging

INTRODUCTION

Force generation by myosin II isoforms is fundamental to the function of all eukaryotic cells. In addition to the well-known role of myosin II in generating muscle contraction, nonmuscle myosin II (NMII) isoforms are responsible for generating the mechanical forces that power cell division, cell motility, membrane remodeling during endocytosis and exocytosis, and embryo morphogenesis (Betapudi, 2014; Chandrasekar et al., 2014; Milberg et al., 2017; Sellers, 2000; Vicente-Manzanares et al., 2009). Dysregulation of force generation by nonmuscle myosin II can result in or contribute to disease conditions that include muscular dystrophy, cardiomyopathy and metastatic cancer (Heissler and Sellers, 2016; Ma and Adelstein, 2014; Sellers, 2000). In humans, cells express at least one of three known NMII isoforms (IIA, IIB, IIC, heavy chains encoded by *MYH9*, *MYH10* and *MYH14*), which predominantly assemble into bipolar filament assemblies containing ∼15–30 molecules of NMII (Billington et al., 2013). These bipolar filaments use energy generated by ATP hydrolysis to translocate actin filaments, and in so doing generate contractile forces. Recent advances have demonstrated that the localization and activation of NMII are subject to complex regulation (Beach et al., 2017; Beach and Hammer, 2015; Beach et al., 2014; Fenix et al., 2016; Hu et al., 2017; Shutova et al., 2014). However, despite its biological importance, a method for directly visualizing the mechanical forces generated by NMII in living cells is presently lacking.

In vitro measurements have shown that single myosin catalytic domains generate forces of 4–5 pN (Finer et al., 1994). Recently developed Förster resonance energy transfer (FRET)-based tension sensors are well suited to investigate how motor proteins generate and propagate piconewton-scale forces in cells (Freikamp et al., 2016; Grashoff et al., 2010; Guo et al., 2014; Meng et al., 2008). One such sensor, termed the tension sensor module (TSMod), consists of an extensible flagelliform linker peptide flanked by FRET donor and acceptor fluorophores (Grashoff et al., 2010). Tension on TSMod results in the extension of the flagelliform linker and a corresponding decrease in FRET efficiency that can be quantified to yield an estimate of the magnitude of the force (i.e. tension) experienced by the module (Fig. 1A). FRET-based tension sensors have enabled the measurement of traction forces at integrin-based cell–matrix adhesions (Kumar et al., 2016; LaCroix et al., 2018; Nordenfelt et al., 2016), the nuclear LINC complex (Arsenovic and Conway, 2018; Arsenovic et al., 2016), cell–cell adhesions (Baddam et al., 2018; Borghi et al., 2012; Lagendijk et al., 2017; Price et al., 2018) and within the spectrin cytoskeleton (Krieg et al., 2014). FRET-based tension sensors likewise allow the measurement of mechanical tension on the host protein in intact, living model organisms (Krieg et al., 2014; Lagendijk et al., 2017; Meng et al., 2008; Yamashita et al., 2016).

FRET-based methods have also been widely applied to study conformational dynamics in motor proteins, including myosin II (Iwai and Uyeda, 2008; Kasprzak, 2007; Muretta et al., 2015; Shih et al., 2000). Most of these studies were performed *in vitro* using purified, partial domains of skeletal (Muretta et al., 2015), smooth muscle or *Dictyostelium* (Shih et al., 2000; Zeng et al., 2006) myosin II (e.g. heavy meromyosin or the S1 fragment). *In vitro* optical tweezer microscopy experiments have also revealed details of the mechanism by which myosin II generates force (Finer et al., 1994; Spudich, 2001). Conversely, traction force microscopy and laser microdissection approaches can provide

[1]Enabling Technologies Group, Sanford Research, Sioux Falls, SD 57104, USA. [2]Department of Neurobiology, Physiology and Behavior, University of California Davis, Davis, CA 95616, USA. [3]Department of Nanoscience and Nanoengineering, South Dakota School of Mines and Technology, Rapid City, SD 57701, USA. [4]Department of Physics, Indiana University-Purdue University Indianapolis, Indianapolis, IN 46202, USA. [5]Biophysics Program, Stanford University, Stanford, CA 94305, USA. [6]Department of Chemical Biology, Stanford University, Stanford, CA 94305, USA. [7]Department of Physiology and Membrane Biology, School of Medicine, University of California Davis, Davis, CA 95616, USA. [8]Department of Physics and Astronomy, Purdue University, West Lafayette, IN 46907. [9]Department of Pediatrics, University of South Dakota, Sioux Falls, SD 57105, USA.

*Authors for correspondence (liu456@purdue.edu; indra.chandrasekar@sanfordhealth.org)

A.R.D., 0000-0001-6096-4600; I.C., 0000-0003-3822-0570

Handling Editor: Guillaume Jacquemet
Received 20 May 2024; Accepted 24 September 2024

Journal of Cell Science (2024) 137, jcs262281. doi:10.1242/jcs.262281

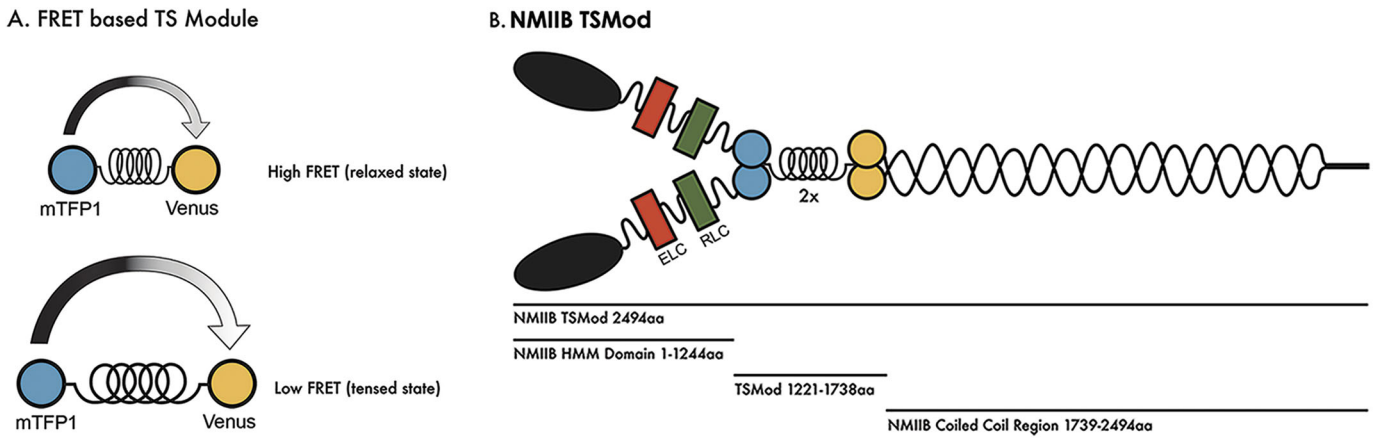

Fig. 1. Design and development of a NMII tension sensor. (A) Schematic of the FRET-based tension sensor module (TSMod) in its relaxed and tensed states. (B) Cartoon illustrating the structural domains of NMIIB TSMod (not drawn to scale).

estimates for actomyosin-generated forces in intact cells (Polacheck and Chen, 2016; Sugita et al., 2011). Recent advances have highlighted the overall force experienced along the actin network (Amiri et al., 2023). However, to our knowledge a direct measurement of NMII-associated forces within the cytoskeleton has not been reported.

In this study, we developed NMIIB tension sensors that report on myosin-generated tension within living cells as a function of FRET donor lifetime or energy exchange ratio. Our measurements reveal that actomyosin-associated forces are dynamic and exhibit spatial and temporal variations in different subcellular regions in both NMIIB-null (NMIIB$^{-/-}$; i.e. with a knockout in exon 2 of the *Myh10* gene) and NMIIB-expressing cells. We anticipate that NMII-based tension sensors might be widely useful for measuring myosin-generated forces in living cells, and in future studies, in intact organisms.

RESULTS

Design and generation of NMIIB tension sensors

NMII is a hexameric motor protein comprising two heavy chains, each of which bind a regulatory and essential light chain (Fig. 1B). The heavy chain is composed of the globular head, which contains both the actin- and ATP-binding sites and a coiled-coil tail domain, which mediates both dimerization and filament assembly (Sellers and Knight, 2007). To generate the NMIIB tension sensor, we inserted TSMod (Fig. 1A) between amino acids (aa) A1220 and L1222, 20 amino acids N-terminal of the conformationally flexible protease recognition site whose cleavage generates heavy meromyosin (Sellers et al., 1981). We predicted that this region of myosin II might be conducive to manipulation without affecting the major structural regions of the heavy chain involved in ATPase activity, light chain binding and bipolar filament assembly.

In addition, we generated control constructs that lacked a functional FRET donor or acceptor fluorophore, termed NMIIB TSMod G73S and the NMIIB TSMod G67S, respectively (Fig. S1B,C). We also generated a construct in which the elastic linker peptide in the TSMod was replaced with a 5-amino-acid (5AA) SGKRS linker that holds the fluorophores in close proximity (NMIIB 5AA), yielding a construct whose FRET efficiency is minimally sensitive to tension (Fig. S1D). To probe the dependence of the force readout on the TSMod insertion site, we designed an alternative NMIIB tension sensor in which TSMod is inserted after the S1 motor domain fragment (1–844 aa) and is hence named NMIIB-S1 TSMod (Fig. S1E).

Characterization of NMIIB tension sensors and control constructs

To evaluate the expression level and localization profile of NMIIB TSMod, we performed transient transfections of NMIIB$^{-/-}$ (null) mouse embryonic fibroblasts (MEFs) and stained for NMIIB and actin filaments (Fig. 2A–D). NMIIB$^{-/-}$ MEFs were generated and characterized as described previously (Chandrasekar et al., 2014). We observed NMIIB TSMod organized into filaments along the cell body and trailing edge that colocalized with the actin cytoskeleton in migrating MEFs (Fig. 2A–D). In human embryonic kidney (HEK293) cells, which express endogenous NMIIB, we also observed the integration of NMIIB TSMod with endogenous NMIIB (Fig. S1G). Immunoblot analysis performed using HEK293 cells transfected with NMIIB TSMod or an N-terminally tagged, donor-only construct (Fig. S1A; mTFP1-NMIIB) showed expression of exogenous mTFP1-NMIIB (255 kDa) or NMIIB TSMod (285 kDa) at levels comparable to endogenous NMIIB (228k Da) (Fig. S1H).

Next, we used NMIIB$^{-/-}$ MEFs to evaluate the ability of NMIIB tension sensors to measure the actomyosin-associated forces in cells. NMIIB FRET values were measured using fluorescence lifetime imaging microscopy (FLIM) with time-correlated single-photon counting (TCSPC) in living cells (see Materials and Methods). Images were processed using PicoQuant software (Symphotime) to determine mTFP1 excited state lifetimes and FRET efficiency values along actomyosin filaments, which we use here as a general term for structures that appear to be stress fibers (Fig. S2). We also perform point measurements by selecting 10–30~0.3×0.3 µm regions of interest (ROIs) on actomyosin filaments to obtain localized, time-resolved FLIM-FRET time series with pixel dwell times of 0.2–0.3 ms, which is not possible when scanning the whole cell (Fig. S2A). Unless specified otherwise, point measurement ROIs were randomly selected along actomyosin filament after scanning a candidate cell.

In the NMIIB$^{-/-}$ MEFs, the donor-only control mTFP1-NMIIB yielded a FRET efficiency of 2.9±8.1% (mean±s.d.), whereas the NMIIB TSMod recorded a FRET efficiency ranging from 25.56±9.19% (Fig. 2E–G). This FRET value is consistent with the presence of mechanical load, as most of it is appreciably less than the FRET efficiency expected (28.6%) in the absence of load, although there was a small percentage of higher FRET values recorded by NMIIB TSMod (Grashoff et al., 2010; Rothenberg et al., 2018). To determine whether the registered FRET efficiency

Journal of Cell Science (2024) 137, jcs262281. doi:10.1242/jcs.262281

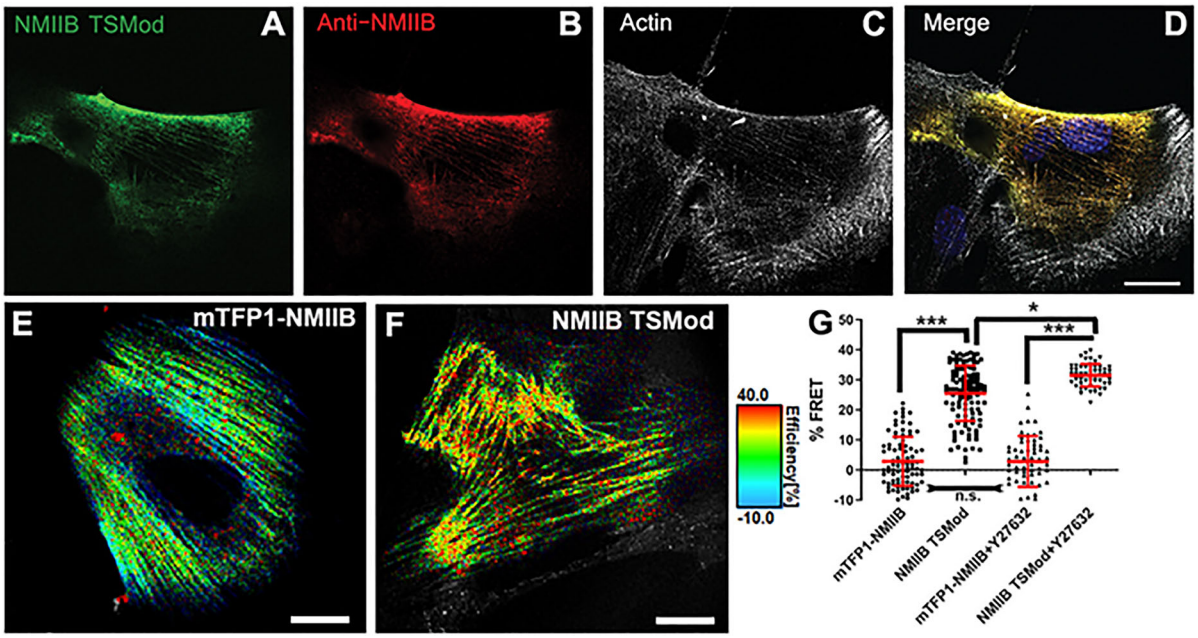

Fig. 2. Functional validation of NMIIB TSMod in NMIIB$^{-/-}$ MEFs. (A–D) NMIIB$^{-/-}$ MEFs transiently expressing NMIIB TSMod (green) showing NMIIB TSMod filaments that are stained with an anti-NMIB antibody (red) and colocalize with actin filaments (white). Images representative of those seen in two repeats. (E–G) Representative FRET images of NMIIB$^{-/-}$ MEFs expressing donor-only control mTFP1-NMIIB (E) and NMIIB TSMod (F) constructs. ROI measurements were performed along the actomyosin filaments in living cells expressing mTFP1-NMIIB (E,G) (n=112 ROIs from 26 cells from three independent replicates) or NMIIB TSMod (F,G) (n=136 ROIs from 22 cells from three independent replicates). Cells were pretreated with the Rho kinase inhibitor Y27632 in a set of experiments before the measurements. (n=69 ROIs from 12 cells for mTFP1-NMIIB and n=62 ROIs from 15 cells for NMIIB TSMod from three independent replicates). In G, the graph represents the percentage FRET values recorded for each construct under the different experimental conditions, with error bars displaying mean±s.d. The FRET values were derived from ROI FLIM measurements recorded from multiple cells. Statistical analyses using Kruskal–Wallis test with multiple comparisons show significant differences between the control and NMIIB TSMod (***P<0.0001), NMIIB TSMod with or without Y27632 (*P=0.03), but not the donor only control with or without Y27632 treatment (n.s.). Scale bars: 10 µm.

for NMIIB TSMod was indeed dependent on the NMII activity in cells, we treated cells with the Rho-kinase inhibitor Y27632 and then performed FLIM-FRET microscopy. Cells expressing the donor-only control mTFP1-NMIIB pretreated with Y27632 yielded an apparent FRET efficiency of 2.88±8.44% (mean±s.d.), which was very similar to the apparent percentage FRET recorded in untreated cells (Fig. 2G). However, NMIIB TSMod-expressing NMIIB$^{-/-}$ MEFs pretreated with Y27632 showed increased FRET efficiency of 31.54±3.77% (Fig. 2G). This indicates that the FRET efficiency reported by NMIIB TSMod is sensitive to phosphorylation-dependent NMII activation. We also assessed the phosphorylation status of myosin light chain (MLC, encoded by *Myl9*) using the anti-phospho-(p)MLC antibody that detects the phosphorylated serine 19 (pSer19), a crucial MLC phosphorylation site for activation of NMII. Untransfected NMIIB$^{-/-}$ MEFs as well as NMIIB$^{-/-}$ MEFs transfected with mTFP1-NMIIB or NMIIB TSMod were fixed and stained with anti-pSer19 MLC antibody. We observed positive pMLC staining and colocalization of pSer19 MLC with mTFP1-NMIIB filaments (Fig. 3A–C) as well as NMIIB TSMod filaments (Fig. 3D–F) in the respective cells. Cells also show regions of pMLC staining without respective exogenous constructs that indicate endogenous NMIIA filaments (Vicente-Manzanares et al., 2011). Untransfected cells also showed phospho-S19 staining given that these cells express NMIIA that interacts with and shares the same MLC for its regulation (Fig. 3G–I). We also assessed focal adhesions in NMIIB$^{-/-}$ MEFs expressing NMIIB TSMod and mTFP1-NMIIB along with untransfected cells using an anti-paxillin antibody, which showed no differences between conditions (Fig. S3).

Next, to assess any differences in the filament turnover rates in living cells, we performed fluorescence recovery after photo bleaching (FRAP) experiments. Cells expressing mTFP1-NMIIB or NMIIB TSMod were subjected to photo bleaching at a selective region of interest (ROI) on the NMII filament structure, and the recovery of fluorescence was tracked for up to 500 s. mTFP1-NMIIB and NMIIB TSMod both had similar recovery rates with the $t_{1/2}$ at 199.2±47.8 s and 226.8±38.02 s, respectively, in NMIIB$^{-/-}$ MEFs (mean±s.d.) (Fig. S4). Taken together, these experiments indicate that NMIIB TSMod can report on actomyosin-associated forces in living cells, and that its molecular characteristics are similar to wild-type NMII.

We used human HEK293 and osteosarcoma cells (U2OS) to validate NMIIB TSMod in cells that also express endogenous NMIIB. In HEK293 cells, the donor-only control mTFP1-NMIIB showed a FRET efficiency of 3±4% (mean±s.d.), which is indistinguishable from zero (Fig. 4A,E). The NMIIB TSMod, yielded a FRET efficiency of 15±8% (Fig. 4B,E). As predicted, the NMIIB-5AA registered the highest FRET efficiency of 34±9% compared to other controls and NMIIB TSMod (Fig. 4C,E). NMIIB TSMod G67S, which lacks a functional FRET acceptor, yielded an apparent FRET efficiency of 4±5% (Fig. 4D,E).

In U2OS cells, NMIIB TSMod yielded a FRET efficiency of 18±9% (mean±s.d.) (Fig. 5). In these cells the FRET efficiencies of the control constructs, NMIIB TSMod G67S, mTFP1-NMIIB, and NMIIB-5AA were 4±5%, 5±5% and 42±3%, respectively (Fig. 5). Thus, FRET measurements were consistent across the two cell lines.

Finally, we assessed NMIIB-S1 TSMod, which was designed to report on the tension generated by a single head of NMIIB. HEK293 cells expressing NMIIB-S1 TSMod yielded a FRET efficiency of

Journal of Cell Science (2024) 137, jcs262281. doi:10.1242/jcs.262281

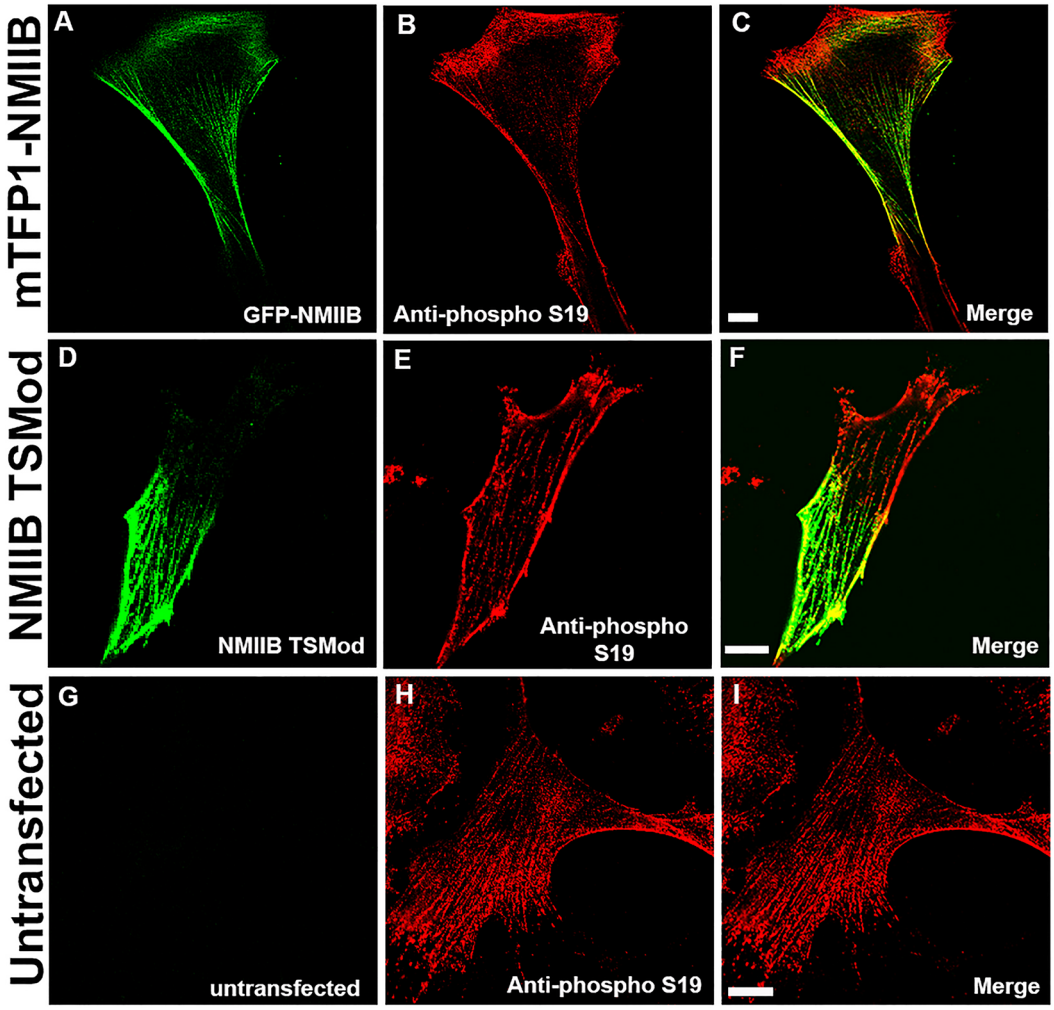

Fig. 3. NMIIB TSMod filaments colocalizes with phosho-MLC in NMIIB$^{-/-}$ MEFs. (A–F) NMIIB$^{-/-}$ MEFs were transiently transfected with mTFP1-NMIIB or NMIIB TSMod, and fixed and stained with anti-phospho-MLC (pSer19) antibody. (A–C) Cells expressing mTFP1-NMIIB show myosin II filaments (green) that are also stained with pMLC antibody (red), colocalization is apparent in regions of the cell in the merged image. Other regions with pMLC staining indicate NMIIA isoform which also shares the light chain. (D–F) Cells expressing NMIIB TSMod show filaments (green) that colocalize with pMLC (red) filaments. Other regions with pMLC staining indicate NMIIA isoform which also shares the light chain. (G–I) Untransfected NMIIB$^{-/-}$ MEFs were stained with anti-pMLC antibody (red) indicate the presence of Ser19 staining; these cells express endogenous NMIIA and pMLC is a light chain for both NMIIB and NMIIA isoforms. Representative images from three independent replicates are shown. Scale bars: 10 µm.

22±4% (mean±s.d.) (Fig. S5). The higher average FRET efficiency compared to NMIIB TSMod is consistent with a lower degree of average tension, perhaps measured only from a single head domain of NMII molecule. An NMIIB-S1 TSMod dark acceptor mutant served as a control construct and yielded low FRET efficiency, as anticipated (Fig. S5).

To evaluate the possibility that FRET values observed for NMIIB TSMod might be influenced by intermolecular FRET within NMII bipolar filament assemblies, we co-transfected HEK293 cells with NMIIB-TSMod G67S and the NMIIB-TSMod G73S, which lack functional FRET acceptor and donor fluorophores, respectively (Fig. S6). FLIM-FRET measurements yielded a FRET efficiency of 2±5% (Fig. S6), indicating that intermolecular FRET was negligible.

Inhibition of NMII motor activity significantly increases the FRET efficiency of NMIIB TSMod

We performed FLIM measurements on HEK293 cells expressing NMIIB TSMod before and after treatment with S-nitro-blebbistatin, which inhibits myosin motor activity directly, or ML-7, which downregulates myosin contractility by inhibiting its activating kinase myosin light chain kinase (MLCK) (Kovacs et al., 2004; Lucas-Lopez et al., 2008; Saitoh et al., 1987). In blebbistatin-treated cells, the FRET efficiency for NMIIB TSMod increased to 27±1% (mean±s.d.) (Fig. 6B,G) compared to the 18±3% recorded before blebbistatin treatment (Fig. 6A,G). ML-7 treatment led to a comparable increase in FRET efficiency to 28±3% (Fig. 6C,G). We also generated a motor domain mutant, NMIIB TSMod R709C, that decreases the maximal ATPase activity to 29% and abolishes the ability of the mutant myosin to translocate actin (Kim et al., 2005). Cells expressing NMIIB TSMod R709C exhibited an average FRET efficiency of 25±4%, which was significantly higher than that in cells expressing NMIIB TSMod (P<0.0001, Mann–Whitney test) (Fig. 6D). Acute inhibition of NMII ATPase activity using S-nitro-blebbistatin or ML-7 did not alter the FRET efficiencies for NMIIB TSMod R709C (Fig. 6E,F,H). Together, these data indicate that FRET values reported by NMIIB TSMod are sensitive to perturbations that alter force generation by NMII.

Journal of Cell Science (2024) 137, jcs262281. doi:10.1242/jcs.262281

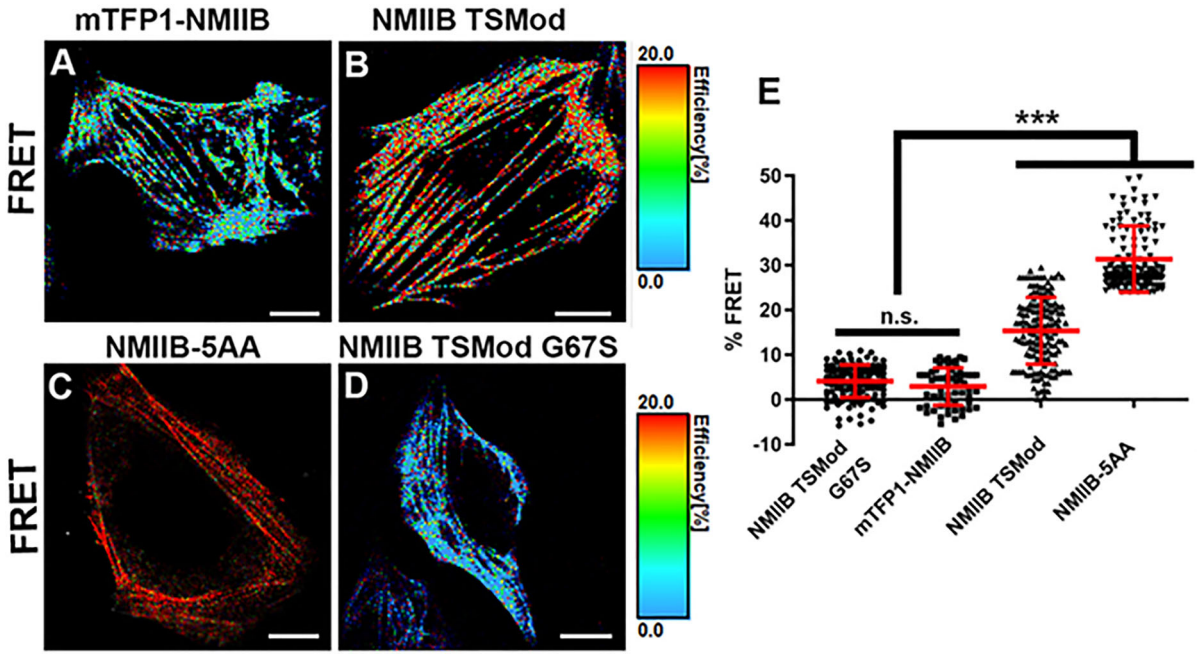

Fig. 4. Validation of NMIIB TSMod within the actomyosin filaments in HEK293 cells. (A–D) Representative FRET images of HEK293 cells expressing NMIIB TSMod and control constructs. ROI measurements were performed along the actomyosin filaments in living cells expressing mTFP1-NMIIB [donor only control (A)] and the NMIIB TSMod G67S [dark acceptor control (D)] show lower FRET (%) compared to NMIIB TSMod (B). NMIIB-5AA, a FRET control that measures energy transfer between fluorophores at close proximity, shows high FRET efficiency as expected (C). ROIs n=66, n=136, n=154, n=167, respectively, from 15, 32, 19, and 25 cells from 3, 3, 7, 5 independent replicates. (E) Graph representing FRET percentages (%) recorded for each construct with error bars displaying mean±s.d. Statistical analyses using Kruskal–Wallis test with multiple comparisons show significant differences (***P<0.0001) between all parameters, except between controls NMIIB TSMod G67S and mTFP1-NMIIB (n.s., P>0.9999). Scale bars: 10 µm.

Changes in actomyosin-associated forces in U2OS cells with and without pharmacological perturbations can be detected using NMIIB TSMod

Actomyosin-associated forces regulate various aspects of cell migration (Murrell et al., 2015). We challenged U2OS cells expressing NMIIB TSMod and Ruby3–Lifeact under conditions that would either increase (hypotonic pressure) or decrease (Y27632 treatment) tension generated by myosin using live confocal and ratiometric imaging experiments. Data was acquired by exciting the mTFP1 donor fluorophore and simultaneously recording both the donor and acceptor emitted light. This imaging approach is much more readily available, and the feasibility of this approach is crucial for broader use of this sensor. Co-expression of NMIIB TSMod and Ruby3-Lifeact enabled real time tracking of the sensor with F-actin using orthogonal fluorophores.

U2OS cells were imaged for 20 min at 2 frames per minute. A base medium of 25 mM glucose Krebs Ringer buffered saline was perfused at a rate of 200ul a minute over the cells (Huang et al., 2024). Treatments were applied using an automated microfluidic distributor to maintain an even flow rate as solutions were distributed over cells. Treatment with the ROCK inhibitor Y27632 significantly reduced the average CFP-to-YFP (CFP/YFP) ratio compared to that recorded before treatment, indicating a decrease in the tension generated by NMIIB TSMod (Fig. 7A,B). To strain the F-actin network and stretch the cells, a hypotonic solution with diluted base medium (50% molecular grade water) was used for swelling the cells (Huang et al., 2019; Jaiswal et al., 2019; Phillips et al., 2022). During hypotonic stress, a significant increase in the CFP/YFP ratio was observed compared to the ratio recorded before treatment, indicating that NMIIB TSMod sensor was experiencing strain due to swelling (Fig. 7C,D). Representative images from the experiments are also presented highlighting the colocalization between the CFP, YFP and RFP channels (NMIIB TSMod fluorophores and Ruby3–Lifeact, Fig. 7E–H) and Movie 1.

DISCUSSION

We developed and validated an NMII tension sensor that yielded the first, to our knowledge, direct measurements of forces generated by NMII in living cells. Cellular measurements were obtained both in the presence and in the absence of endogenous NMIIB expression. Validation experiments were performed using both time-domain FLIM and traditional fluorescent protein ratiometric recordings in different cell types including NMIIB$^{-/-}$ MEFs with essential controls to account for the possible contribution of environmental sensitivity, intermolecular FRET, phosphorylation status and ATPase activity (mTFP NMIIB, NMIIB TSMod G67S, NMIIB TSMod G73S and NMIIB TSMod R706C). FRET percentages for NMIIB TSMod were higher in NMIIB$^{-/-}$ MEFs cells than that registered in HEK293 and U2OS, likely a result of variation in NMIIB filament dynamics in cells with and without endogenous protein expression. Measurements in which myosin activity was reduced using either Y27632, blebbistatin or ML-7 yielded FRET efficiencies in good agreement with the expected FRET values for TSMod under low motor activity and negligible tension (Figs 2, 6, 7) (Grashoff et al., 2010; Rothenberg et al., 2018).

The R709C mutation is known to decrease NMIIB actin-activated ATPase activity to 29% that of wild-type NMIIB, and to completely block actin translocation in an *in vitro* motility assay (Kim et al., 2005). Consistent with these observations, the crystal structure of NMIIB indicates that this mutation likely blocks allosteric communication between the ATPase site and the lever arm (Munnich et al., 2014). Interestingly, the R709C motor domain

Journal of Cell Science (2024) 137, jcs262281. doi:10.1242/jcs.262281

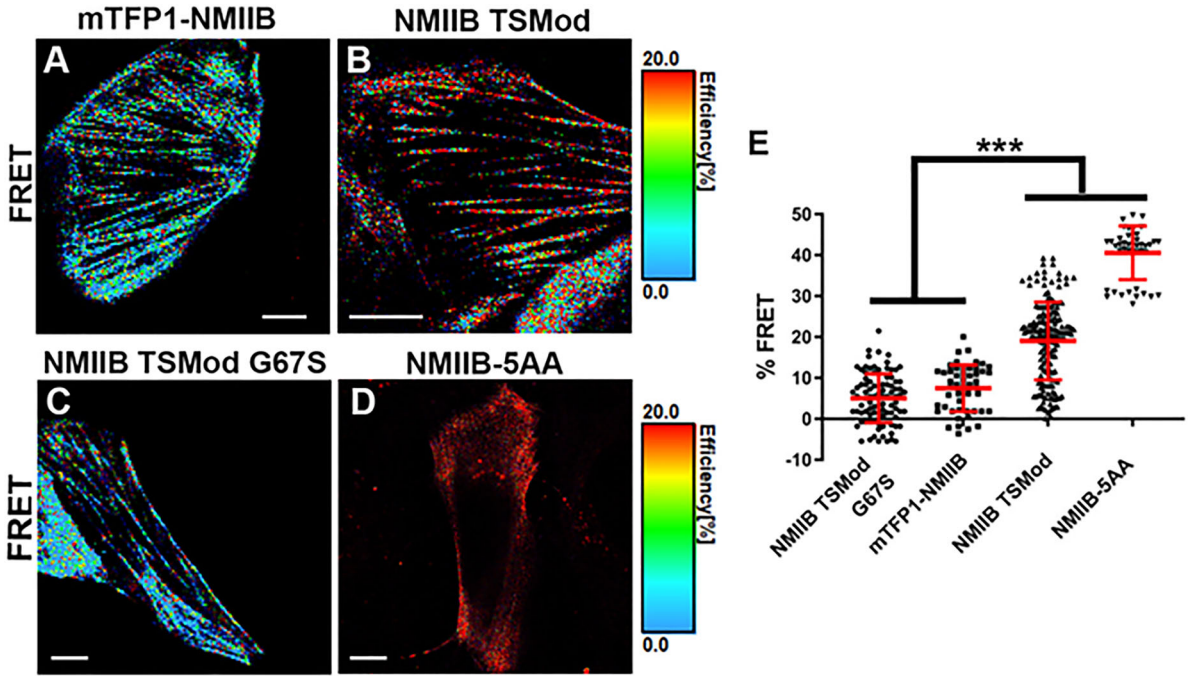

Fig. 5. Validation of NMIIB TSMod in U2OS cells. (A–D) Representative FRET images of U2OS cells expressing the NMIIB TSMod and the control constructs. (E) Graph representing FRET percentage (%) for all the constructs with error bars displaying mean±s.d. ROI measurements performed along actomyosin filaments in live cells expressing mTFP1-NMIIB (A,E) and the NMIIB TSMod G67S (C,E) show lower FRET efficiencies (%) compared to NMIIB TSMod (B,E). NMIIB-5AA, a FRET control that measures energy transfer between fluorophores at close proximity, shows low lifetimes and high FRET efficiencies (D,E). ROIs, *n*=50, 93, 177 and 45 from 15, 19, 28, and 13 cells, respectively, from 3, 3, 5, and 3 independent replicates). ***P<0.0001 between all parameters, except between controls NMIIB TSMod G67S and mTFP1-NMIIB (P>0.9999). Scale bars: 10 µm.

mutant was sufficient to rescue cytokinesis defects in both NMIIB-depleted COS-7 cells and cardiac myocytes (Ma et al., 2012); an observation interpreted as indicating that NMIIB R709C could maintain tension, but not generate active force. In agreement with this, we observed a FRET efficiency for NMIIB R709C of 25±3.6% (mean±s.d.), suggestive of the presence of a small amount of tension on NMIIB TSMod R709C molecules. Consistent with previous interpretations, this tension (if present) is unlikely to require the ATPase activity of the mutant myosin, as treatment with S-nitro-blebbistatin or ML-7 did not alter the FRET efficiencies for NMIIB TSMod R709C.

It is likely that further optimization will yield myosin-based tension sensors with expanded sensitivity and applicability. New sensor modules with improved molecular springs might improve the mechanical sensitivity of the current sensor, which is limited to 1–6 pN (LaCroix et al., 2018; Ringer et al., 2017). Recent studies have also begun to highlight the role mechanical forces play in influencing fluorescent protein dynamics and intensity during stimulation (Shoyer et al., 2024). Therefore, the state of the fluorophores under mechanical strain must be considered and accounted for before any direct translation of FRET ratios into intracellular force representations while using NMIIB TSMod. In addition, future experiments that are outside the scope of the current study, such as utilizing purified NMIIB TSMod protein coupled with an optical trap would be essential for developing a force calibration curve to accurately measure actomyosin associated force and tension. This *in vitro* approach can also facilitate assessing the force differences between the NMIIB-S1 TSMod and NMIIB TSMod. We hypothesize that the NMIIB-S1 TSMod, which is functional solely through one motor head, will be excluded from bulk strain generated along the actomyosin network. Analysis of NMIIB-S1 TSMod protein using *in vitro* assays in parallel with NMIIB TSMod has the potential to unravel the relationship between the number of myosin hexamers and actomyosin associated force as a function of the motor heads.

The current sensor design can be likewise extended to NMIIA, the other major NMII isoform in most cells. Complementary NMIIA and NMIIB sensors will likely be useful in clarifying how the two isoforms differentially regulate cytoskeletal organization and force generation in a variety of physiological contexts (Murrell et al., 2015; Vicente-Manzanares et al., 2011). Finally, it will be of considerable interest to translate the current sensor designs to model organisms, for example *Drosophila* and *C. elegans,* to directly visualize myosin-driven forces during embryogenesis.

MATERIALS AND METHODS

Generation of NMIIB tension sensors and control constructs

Infusion Cloning (Clontech cat. # 638910) was used for DNA manipulation unless otherwise specified. The human *MYH10* (NMIIB) coding sequence was amplified using an NMIIB–GFP plasmid generated in the laboratory of Dr Robert Adelstein, as used in our previous work (Chandrasekar et al., 2014). The NMIIB coding sequence was amplified with primers *PCDNA3IIB FL F* and *PCDNA3IIB FL R* (primers sequences can be seen in Table S1) and inserted between EcoR1 and Apa1 of the PCDNA3 multiple cloning site to generate NMIIB-pCDNA3. A unique XBA1 restriction site beginning at base pair 3663 in the NMIIB coding sequence was used to linearize the NMIIB-pCDNA3 construct. The TSMod Coding sequence was amplified from Addgene plasmid #26021 (deposited by the Schwartz laboratory). Primers *TSMod XBA1 F* and *TSMod XBA1 R* were used to amplify the TSMod sequence and it was inserted into the XbaI linearized NMIIB-pCDNA3 construct to generate the NMIIB TSMod construct.

Journal of Cell Science (2024) 137, jcs262281. doi:10.1242/jcs.262281

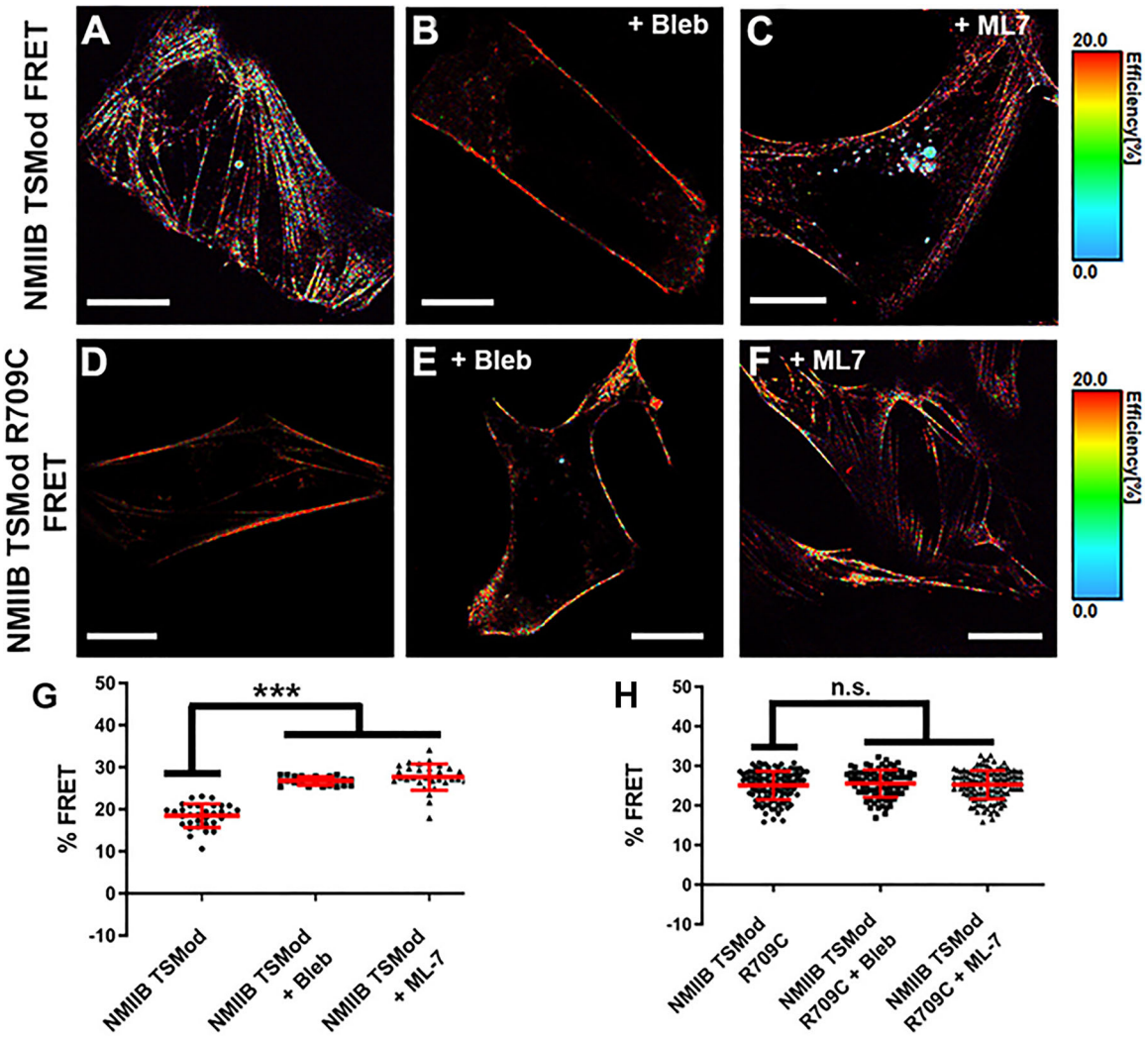

Fig. 6. Inhibition of motor activity increases FRET efficiency for NMIIB TSMod. (A–C) Representative FRET images of HEK293 cells expressing NMIIB TSMod before and after treatment with S-nitro-blebbistatin or ML-7. (D–F) Representative FRET images of HEK293 cells expressing NMIIB TSMod R709C before and after treatment with S-nitro-blebbistatin or ML-7. (G) Graph represents FRET percentage (%) with error bars displaying mean±s.d. from ROI measurements performed along actomyosin filaments in live cells expressing NMIIB TSMod, show increased FRET percentages after 15 min treatment with S-nitro(–) blebbistatin or ML-7 (ROIs *n*=33, 24, 30 from 8, 6, and 9 cells, respectively, from three independent replicates). (H) Graph showing FRET percentage (%) with error bars displaying mean±s.d. from ROI measurements performed along actomyosin filaments in live cells expressing NMIIB TSMod R709C. Treatment with S-nitro(–) blebbistatin (E) or ML-7 (F) did not yield statistically significant increases in FRET efficiency (ROIs *n*=119, 85, 132 from 15, 16 and 23 cells, respectively, from five independent replicates). Statistical analysis using Kruskal–Wallis test with multiple comparisons shows significant differences between untreated and drug treated cells for NMIIB TSMod (***P<0.0001) but not for NMIIB TSMod R709C (n.s., P>0.9999). Scale bars: 10 µm.

NMIIB TSMod control constructs

mTFP1-NMIIB was generated by amplification of NMIIB coding sequence using primers *ICCP170* and ICCP171 inserted into mTFP1-NMIIA (Addgene #55501) replacing NMIIA. Constructs were verified by sequencing analysis.

Three NMIIB TSMod mutant constructs were generated for validation purposes. NMIIB TSMod T (G73S), harboring a point mutation that renders mTFP1 inactive, NMIIB TSMod V (G67S) which renders the Venus fluorophore inactive and NMIIB-R709C (an NMIIB motor domain mutant). Point mutants were generated using the NEB Q5 site-directed mutagenesis kit and protocol (New England Biolabs #E0552S). NMIIB TSMod T (G73S) was generated using primer pair *ICCP269* and *ICCP270* (Table S1). NMIIB TSMod V (G67S) was generated using primer pair *ICCP304* and *ICCP305* (Table S1). NMIIB-R709C TSMod was generated using primer pair *ICCP259** and *ICCP260** (Table S1). To generate NMIIB-5AA, the 40-residue molecular spring in the TSMod was replaced with a 5 amino acid SGKRS linker between the mTFP1 and Venus fluorophores. The NEB Q5 kit polymerase and protocol was used with primers *ICCP294* and *ICCP295* (Table S1) to inversely amplify the entire NMIIB-TSMod plasmid sequence lacking the 40-residue molecular spring region. Homologous 15 bp overhangs on the 3′ end of the inverse PCR primers were ligated following the NEB T4 ligation protocol (New England Biolabs # M0202S) to introduce the 5AA sequence. Constructs were verified by sequencing analysis.

NMIIB-S1 TSMod was generated as described below. The human coding sequence for MYH10 gene was derived from Addgene plasmid #11348 (Wei and Adelstein, 2000). The NMIIB coding sequence was then inserted into pEGFP-N3 between the KpnI and NotI sites, which also removed the parent vector GFP tag. TSMod (Grashoff et al., 2010; Borghi et al., 2012) was cloned into the NMIIB sequence at the beginning of the rod tail domain (between L845 and Q846) using BspEI and SpeI cloning sites engineered into the sequence. We used a TSMod variant that uses mTFP1 and mEYFP as the FRET donor and acceptor, respectively, attached to the NMIIB coding sequence by short linkers encoding GlyGlyAlaGlyAlaGly to aid in fluorophore folding. Additionally, PacI and AscI restriction sites between the fluorophores and the flagelliform sequence were inserted to aid in the

Journal of Cell Science (2024) 137, jcs262281. doi:10.1242/jcs.262281

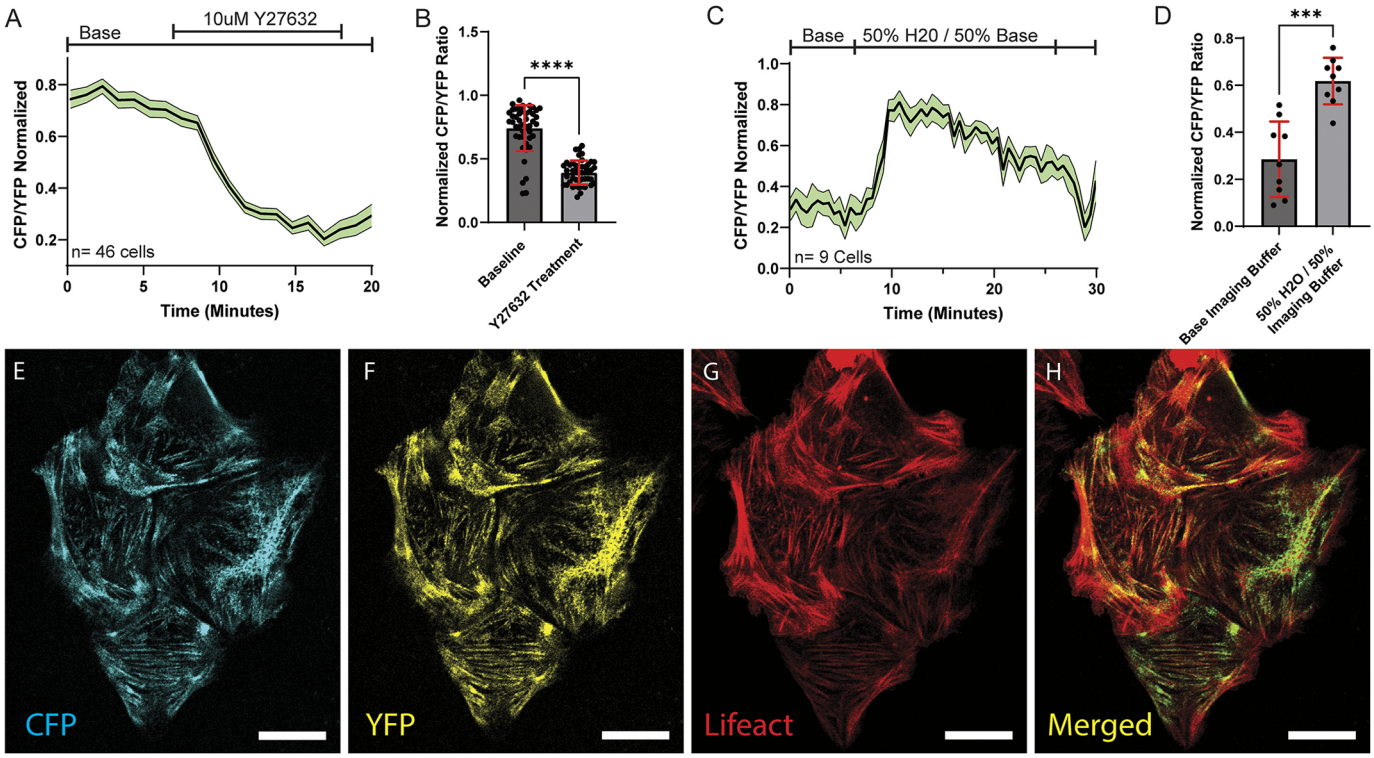

Fig. 7. Changes in actomyosin-associated forces in U2OS cells with and without pharmacological perturbations can be detected using NMIIB TSMod. (A,B) The ROCK inhibitor Y27632 treatment results in a significant decrease (paired two-tailed Student's *t*-test, $P<0.0002$) in tension detected using the NMIIB TSMod sensor ($n=46$ cells from five independent replicates). (C,D) Increasing osmotic pressure by introducing a hypotonic environment through the addition of water to the imaging buffer results in a significant increase (paired two-tailed Student's *t*-test, $P<0.0010$) in tension along the stretching cytoskeleton ($n=9$ cells from three independent replicates). Shaded area in A and C is s.e.m., error bars in B,D display mean±s.d. (E–H) Representative images show NMIIB TSMod fluorophores (E,F) and the actin cytoskeleton (G). Merged image (H) demonstrates colocalization of actin cytoskeleton and NMIIB TSMod (YFP image pseudo colored green) in cells during live imaging. Images representative of those seen in five repeats. Scale bars: 20 µm.

construction of control constructs. The NMIIB-S1 TSMod domain sequence is thus NMIIB (catalytic domain and lever arm)-linker-BspEI-mTFP1-PacI-flagelliform-AscI-mEYFP-SpeI-linker-NMIIB (coiled coil domain). A dark acceptor version of NMIIB-S1 TSMod was made by introducing the mutation Y67G (relative to the fluorophore sequence) in mEYFP (Takanaga and Frommer, 2010).

Cell culture conditions and stable cell generation

HEK293, U2OS, wild-type (WT) MEFs and MEF NMIIB-knockout (KO) cells (ATCC; Chandrasekar et al., 2014) were cultured in DMEM (Corning #10013CV) supplemented with 10% FBS (Atlanta Biologicals# S11150H) and 1× concentration of penicillin-streptomycin (Corning #30002Cl). Lipofectamine 2000CD (Life Technologies #12566014) with the corresponding protocol was used to transfect the cell lines. To generate cells stably expressing these constructs, medium supplemented with 500 µg/ml G418 sulfate solution (Corning #30234CR) was used on cells 2 days after transfection. After a 10-day G418 selection, GFP-positive cells were sorted using the FACSjazz cell sorting system (BD Biosciences) to obtain a pure population. G418 selection pressure was maintained while culturing cells. To validate the function of the tension sensor, live cells were treated with S-nitro-blebbistatin (30 µM for 15 min), ML-7 (30 µM for 15 min) and Y27632 (30 µM for 30 min). These drugs were all acquired from Calbiochem (San Diego, CA; now Millipore, Sigma)

Immunocytochemistry

35 mm Fluorodish glass bottom dishes (World Precision Instruments #FD35-100) were coated overnight with human fibronectin (Corning #CB 40008). Each dish was rinsed with sterile phosphate-buffered saline (PBS; Corning# 21040CV) prior to seeding cells on dishes. 150,000 cells were seeded onto each dish for immunocytochemistry. At 18 to 24 h after seeding, cells were transfected as described above and prepared for immunocytochemistry. Cells were fixed for 15 min at room temperature with 4% paraformaldehyde (Electron Microscopy Sciences #15710) in cacodylate buffer (0.1 M cacodylate salt, 10 mM $CaCl_2$, 10 mM $MgCl_2$, pH 7.4). The solution was warmed to 37°C prior to addition to cells. Cells were rinsed three times with cacodylate buffer followed by PBS. Cells were permeabilized by incubating in 0.1% Triton-X-100 in PBS for 10 min. Blocking solution (5% goat serum, 4% fish gelatin, 1.2% BSA in phosphate buffered saline) was applied for 1 h at room temperature. After blocking, primary anti-NMIIB rabbit antibody (Biolegend #909901) was applied at a 1:500 dilution for 1 h at room temperature. Secondary antibodies and dyes used were Anti-rabbit-IgG conjugated to Alexa Fluor 567 (Life Technologies #A-11011) at a 1:500 concentration and Alexa Fluor 647–phalloidin at a 1:100 concentration (Life Technologies #A22287). Each secondary antibody was incubated with cells for 1 h at room temperature. After final PBS washes, cells were mounted using Vectashield with DAPI (Vector Labs #H-1200). Other antibodies utilized were anti-phospho-MLC Ser19 (1:200, Cell Signaling Technology #3671) and anti-paxillin antibody [Y113] (1:500, Abcam, Catalog #Ab32084). Cell lines HEK293 (CRL-1573) and U2OS (HTB-96) were purchased from ATCC. $NMIIB^{-/-}$ MEFs were harvested from NMIIB-null mice (Bridgman et al., 2001; Tullio et al., 2001) embryonic tissue as previously described (Chandrasekar et al., 2014). All procedures involving use of animals have been approved by the Washington University Animal Studies Committee.

Western blot analysis

HEK293 cells transfected with NMIIB TSMod and mTFP1-NMIIB were lysed 48 h after transfection. Cells were lysed with ice-cold NMIIB lysis buffer (150 mM NaCl, 50 mM Tris base, 5 mM $MgCl_2$, 2 mM ATP, 0.1% NP-40, 10% glycerol). After lysis, protein levels were quantified using the colorimetric BCA assay (Pierce #23225). 10 µg of protein lysate was loaded on a 5% Tris glycine polyacrylamide gel and protein separation occurred at

Journal of Cell Science (2024) 137, jcs262281. doi:10.1242/jcs.262281

110 volts in 25 mM Tris-HCl, 192 mM glycine and 0.1% SDS running buffer (pH 8.3). Proteins were transferred to PVDF membranes at 100 volts for 1 h in ice cold 25 mM Tris-HCl, 192 mM glycine transfer buffer (pH 8.3). Membranes were rinsed briefly in Tris-buffered saline with Tween 20 (TBST; 50 mM Tris-HCl, 150 mM NaCl, pH 7.5 and 0.1% Tween 20). Membranes were blocked in 5% milk in TBST for 1 h at room temperature with agitation. Anti-NMIIB rabbit (Biolegend #909901) primary antibody was diluted 1:1000 in 5% milk in TBST and placed on membrane overnight in a rocker platform at 4°C. Membranes were rinsed three times with TBST. Anti-rabbit-IgG conjugated to HRP secondary antibody (Jackson Immunoresearch #711-035-152) was diluted 1:10,000 in 5% milk in TBST and incubated with the membrane for 1 h at room temperature with gentle agitation. The membrane was then rinsed three times with TBST and visualized with UV lighting after applying the chemiluminescent substrate to the membrane (EMD Millipore #WBLUF0100). Uncropped images of western blot sin this paper are provided in Fig. S7.

Wide-field fluorescent imaging

General wide-field fluorescent imaging was performed with a Nikon A1-TIRF microscope (Sanford Research) and images were processed and analyzed by ImageJ.

Confocal FLIM-FRET imaging

A customized fluorescence lifetime imaging microscopy (FLIM) was used to obtain the lifetime of the donor molecule, which was then utilized for the quantification of FRET efficiency. The FLIM system was developed using a Olympus Fluoview 1000 laser scanning confocal microscope; a picosecond pulsed laser with the wavelength of 450 nm (LDH-D-C-450, Picoquant) was coupled with the FV1000 laser scanning module, and equipped with an oil-immersion objective (60×, 1.3 NA). The excited fluorescent signal was collected by the same objective and was filtered by a band-pass filter 490-40 (ET490/40X, Chroma) before entering a photon counting detector (PD-100-CTC, MPD). All signals were recorded in the time-correlated single-photon counting (TCSPC) mode with a data acquisition board (TimeHarp 260, Picoquant). FLIM image acquisition, lifetime calculation and the FRET conversion were performed in the software SymPhoTime 64 (Picoquant), as described below.

Simultaneous NMIIB TSMod and F-actin live imaging and pharmacological perturbations

A Nikon A1R scanning confocal microscope was used to acquire mTFP1 (CFP) and Venus A206 (YFP) signal from the NMIIB TSMod simultaneously during mTFP1 stimulation with a 445 nm laser line. Detection of both channels was achieved using a dedicated gallium arsenide phosphide (GaAsP) detector for both the CFP and YFP emission, respectively. Cells were transfected with a Ruby3–Lifeact expression plasmid in parallel to the NMIIB TSMod to facilitate live imaging of F-actin with the myosin II tension sensor. A 561 nm laser line with a filter set designed to prevent spectral bleed through from the YFP channel was utilized for imaging. Data was acquired using a high-speed resonant scanner, with 32× averaging of each channel and each frame. Solutions delivered during live imaging experiments involved the continuous perfusion of 25 mM glucose Krebs Ringer buffer at a rate of 200 µl per minute. Steady flow was maintained using the Elveflow microfluidics system, with different treatments adjusted using the Mux distributor. 10 µM Y27632 in buffer was flowed in to follow the effect of the drug treatment.

Lifetime calculation

The fluorescent lifetime of the donor mTFP1 molecule was obtained by analyzing the time-correlated decay curves in the SymPhoTime 64 software. Details about the TCSPC principle and data acquisition are as previously described (O'Connor, 1984). We applied a multi-component (N) exponential decay function, $I = \sum_{i}^{N} A_i exp(-t/\tau_i)$, to numerically fit the TCSPC decay curve of each pixel. Here, τ_i is the lifetime of the i^{th} component and A_i is its amplitude. A two-component model was applied to fit all the data acquired in this work. Finally, we color map the fluorescent intensity image and calculate the FRET efficiency with the averaged fluorescent lifetime, which is calculated as $\tau_{avg} = \sum A_i\tau_i / \sum A_i$. FLIM images were obtained with this model in SymPhoTime 64. For statistical comparison of the FLIM/FRET data, regions of interest (ROIs) were selected and the TCSPC curves of the ROI were fitted as above.

FRET calculation

In FRET interactions, the non-radiative energy transfer from the excited donor fluorophore to the acceptor reduces the fluorescence quantum yield of the donor. Such a reduction of quantum yield leads to both reduced fluorescence intensity and lifetime of the donor molecule. The intensity-based FRET measurements are well adopted primarily due to the flexibility of instrumentation, its analysis requires either the bleaching/depletion of acceptor molecules or sophisticated calibration of multi-channel sensitized emission. The lifetime-based FRET analysis offers the highest FRET sensitivity and simplicity, as only two samples (donor only and donor–acceptor) are necessary to perform effective and reliable FRET measurements. Both methods (intensity and lifetime-based FRET) have been widely used to quantify the FRET efficiency of the molecular tension sensors in the field (Austen et al., 2015; Borghi et al., 2012; Cost et al., 2019; Fangjia Li, 2019; Grashoff et al., 2010; Kumar et al., 2016; Meng and Sachs, 2011, 2012; Meng et al., 2008; Morimatsu et al., 2013; Ng et al., 2014).

In our work, the FRET efficiency of the TS module, µ, was calculated based on the lifetime of the donor molecule:

$$\mu = 1 - \frac{\tau_{AD}}{\tau_D}, \quad (1)$$

where τ_{AD} is the fluorescence lifetime of the donor molecule in the presence of the acceptor, and τ_D is the fluorescence lifetime of the donor molecule without the acceptor. The value of τ_{AD}/τ_D is obtained by fitting the decay curve in the software Symphotime (Picoquant) (Jing Liu et al., 2014; Vidi et al., 2014). Because the microenvironment in cells, such as pH, ions, and refractive index, might alter the fluorescent lifetime of the FRET donor, even for the same construct, it is very common to obtain slight varying values depending on cell type. To this end, we have conducted individual measurements of the donor lifetime in each cell line.

Furthermore, we constructed two versions of NMIIB protein lacking the acceptor to use as a donor-only control, both of which recorded the same fluorescence lifetime (2.74 ns). We replaced the sensor module with a 5-amino-acid (5AA) linker to function as a positive FRET control. The 5AA sample exhibits a FRET efficiency of 50%, which agrees very well with the theoretical expectation of a donor and acceptor molecule at this proximity. All FRET images and efficiencies were calculated based on this donor-only lifetime value.

FRAP experiments and analysis

FRAP experiments were conducted on the same confocal microscope (Olympus FV1000). The confocal microscope has a second galvo-scanning system equipped with a high-power laser (532 nm) as the photobleaching beam. After obtaining the fluorescence image of the cell from the main scanner (mTFP1 channel), a region of interest (ROI) was selected and the photobleaching beam was applied to the ROI to induce the photobleaching. Immediately after the photobleaching, a time-course image acquisition with the main scanner (mTFP1 channel) was taken to record the recovery of the fluorescent intensities at the photobleached region. Quantitative FRAP analysis was implemented in ImageJ. Briefly the averaged intensities of the bleached regions were calculated and plotted with respect to the time, where the background and natural photobleaching effect during the time-course fluorescent image acquisition were corrected. The half-time of the fluorescent recovery was recorded for quantitative comparisons.

Statistical analysis

Figure legends have the description of number of ROIs and cells used for analysis in each experiment. Statistical significance was evaluated using GraphPad Prism and described in each figure legend.

Acknowledgements
We thank Sanford Histology and the Imaging core at Sanford Research.

Competing interests
The authors declare no competing or financial interests.

Author contributions
Conceptualization: A.R.D., J.L., I.C.; Methodology: R.G.H., D.K., F.L., M.Z., D.R., A.J.P., K.L.O., A.R.D., J.L., I.C.; Software: D.K., F.L., M.Z., A.R.D., J.L., I.C.; Validation: R.G.H., D.K., M.Z., D.R., A.J.P., K.L.O., J.L., I.C.; Formal analysis: R.G.H., D.K., F.L., M.Z., K.L.O., J.L., I.C.; Investigation: R.G.H., D.K., M.Z., D.R., A.J.P., K.L.O., A.R.D., J.L., I.C.; Resources: S.J.S., J.L., I.C.; Data curation: D.K., J.L., I.C.; Writing - original draft: J.L., I.C.; Writing - review & editing: R.G.H., D.K., S.J.S., A.R.D., J.L., I.C.; Visualization: R.G.H., D.K., F.L., J.L., I.C.; Supervision: S.J.S., M.O.H., J.L., I.C.; Project administration: J.L., I.C.; Funding acquisition: J.L., I.C.

Funding
Authors would like to acknowledge the funding support from the National Science Foundation EPSCoR program (grant number IIA - 1355423) and by the state of South Dakota to I.C., J.L. and S.J.S., National Institutes of Health (NIH) 1R35GM147412 (J.L.), National Science Foundation (NSF) 2347957 and NSF 2431792 (J.L.), and National Institute of Diabetes and Digestive and Kidney Diseases (NIDDK) R01 DK131020 (I.C.). R.G.H. is supported by NIDDK F31DK132954 and M.O.H. is supported by NIDDK R01 DK110276. Deposited in PMC for release after 12 months.

Data availability
All relevant data can be found within the article and its supplementary information.

First Person
This article has an associated First Person interview with the first author of the paper.

Peer review history
The peer review history is available online at https://journals.biologists.com/jcs/lookup/doi/10.1242/jcs.262281.reviewer-comments.pdf

Special Issue
This article is part of the Special Issue 'Imaging Cell Architecture and Dynamics', guest edited by Lucy Collinson and Guillaume Jacquemet. See related articles at https://journals.biologists.com/jcs/issue/137/20.

References

Amiri, S., Muresan, C., Shang, X., Huet-Calderwood, C., Schwartz, M. A., Calderwood, D. A. and Murrell, M. (2023). Intracellular tension sensor reveals mechanical anisotropy of the actin cytoskeleton. *Nat. Commun.* **14**, 8011. doi:10.1038/s41467-023-43612-5

Arsenovic, P. T. and Conway, D. E. (2018). Using Nesprin tension sensors to measure force on the LINC complex. *Methods Mol. Biol.* **1840**, 59-71. doi:10.1007/978-1-4939-8691-0_6

Arsenovic, P. T., Ramachandran, I., Bathula, K., Zhu, R., Narang, J. D., Noll, N. A., Lemmon, C. A., Gundersen, G. G. and Conway, D. E. (2016). Nesprin-2G, a Component of the Nuclear LINC Complex, Is Subject to Myosin-Dependent Tension. *Biophys. J.* **110**, 34-43. doi:10.1016/j.bpj.2015.11.014

Austen, K., Ringer, P., Mehlich, A., Chrostek-Grashoff, A., Kluger, C., Klingner, C., Sabass, B., Zent, R., Rief, M. and Grashoff, C. (2015). Extracellular rigidity sensing by talin isoform-specific mechanical linkages. *Nat. Cell Biol.* **17**, 1597-1606. doi:10.1038/ncb3268

Baddam, S. R., Arsenovic, P. T., Narayanan, V., Duggan, N. R., Mayer, C. R., Newman, S. T., Abutaleb, D. A., Mohan, A., Kowalczyk, A. P. and Conway, D. E. (2018). The desmosomal cadherin desmoglein-2 experiences mechanical tension as demonstrated by a FRET-based tension biosensor expressed in living cells. *Cells* **7**, 66. doi:10.3390/cells7070066

Beach, J. R. and Hammer, J. A.3rd. (2015). Myosin II isoform co-assembly and differential regulation in mammalian systems. *Exp. Cell Res.* **334**, 2-9. doi:10.1016/j.yexcr.2015.01.012

Beach, J. R., Shao, L., Remmert, K., Li, D., Betzig, E. and Hammer, J. A.3rd. (2014). Nonmuscle myosin II isoforms coassemble in living cells. *Curr. Biol.* **24**, 1160-1166. doi:10.1016/j.cub.2014.03.071

Beach, J. R., Bruun, K. S., Shao, L., Li, D., Swider, Z., Remmert, K., Zhang, Y., Conti, M. A., Adelstein, R. S., Rusan, N. M. et al. (2017). Actin dynamics and competition for myosin monomer govern the sequential amplification of myosin filaments. *Nat. Cell Biol.* **19**, 85-93. doi:10.1038/ncb3463

Betapudi, V. (2014). Life without double-headed non-muscle myosin II motor proteins. *Front. Chem.* **2**, 45. doi:10.3389/fchem.2014.00045

Billington, N., Wang, A., Mao, J., Adelstein, R. S. and Sellers, J. R. (2013). Characterization of three full-length human nonmuscle myosin II paralogs. *J. Biol. Chem.* **288**, 33398-33410. doi:10.1074/jbc.M113.499848

Borghi, N., Sorokina, M., Shcherbakova, O. G., Weis, W. I., Pruitt, B. L., Nelson, W. J. and Dunn, A. R. (2012). E-cadherin is under constitutive actomyosin-generated tension that is increased at cell-cell contacts upon externally applied stretch. *Proc. Natl. Acad. Sci. USA* **109**, 12568-12573. doi:10.1073/pnas.1204390109

Bridgman, P. C., Dave, S., Asnes, C. F., Tullio, A. N. and Adelstein, R. S. (2001). Myosin IIB is required for growth cone motility. *J. Neurosci.* **21**, 6159-6169. doi:10.1523/JNEUROSCI.21-16-06159.2001

Chandrasekar, I., Goeckeler, Z. M., Turney, S. G., Wang, P., Wysolmerski, R. B., Adelstein, R. S. and Bridgman, P. C. (2014). Nonmuscle myosin II is a critical regulator of clathrin-mediated endocytosis. *Traffic* **15**, 418-432. doi:10.1111/tra.12152

Cost, A.-L., Khalaji, S. and Grashoff, C. (2019). Genetically Encoded FRET-Based Tension Sensors. *Curr. Protoc. Cell Biol.* **83**, e85. doi:10.1002/cpcb.85

Fangjia Li, A. C., Shengzhi, L., Andrew, R., Yue, W., Yao, F., Xingyu, Z., Rahual, P., Bai-yan, L., Hiroki, Y. and Jing, L. et al. (2019). Vinculin force sensor detects tumor-osteocyte interactions. *Sci. Rep.* **9**, 5615. doi:10.1038/s41598-019-42132-x

Fenix, A. M., Taneja, N., Buttler, C. A., Lewis, J., Van Engelenburg, S. B., Ohi, R. and Burnette, D. T. (2016). Expansion and concatenation of non-muscle myosin IIA filaments drive cellular contractile system formation during interphase and mitosis. *Mol. Biol. Cell.* **27**, 1465-1478. doi:10.1091/mbc.E15-10-0725

Finer, J. T., Simmons, R. M. and Spudich, J. A. (1994). Single myosin molecule mechanics: piconewton forces and nanometre steps. *Nature* **368**, 113-119. doi:10.1038/368113a0

Freikamp, A., Cost, A. L. and Grashoff, C. (2016). The Piconewton force awakens: quantifying mechanics in cells. *Trends Cell Biol.* **26**, 838-847. doi:10.1016/j.tcb.2016.07.005

Grashoff, C., Hoffman, B. D., Brenner, M. D., Zhou, R., Parsons, M., Yang, M. T., McLean, M. A., Sligar, S. G., Chen, C. S., Ha, T. et al. (2010). Measuring mechanical tension across vinculin reveals regulation of focal adhesion dynamics. *Nature* **466**, 263-266. doi:10.1038/nature09198

Guo, J., Sachs, F. and Meng, F. (2014). Fluorescence-based force/tension sensors: a novel tool to visualize mechanical forces in structural proteins in live cells. *Antioxid Redox Signal.* **20**, 986-999. doi:10.1089/ars.2013.5708

Heissler, S. M. and Sellers, J. R. (2016). Various themes of myosin regulation. *J. Mol. Biol.* **428**, 1927-1946. doi:10.1016/j.jmb.2016.01.022

Hu, S., Dasbiswas, K., Guo, Z., Tee, Y. H., Thiagarajan, V., Hersen, P., Chew, T. L., Safran, S. A., Zaidel-Bar, R. and Bershadsky, A. D. (2017). Long-range self-organization of cytoskeletal myosin II filament stacks. *Nat. Cell Biol.* **19**, 133-141. doi:10.1038/ncb3466

Huang, C., Li, Y. and Wang, H. (2019). The observation of high hypotonicity manipulating cell division. *Heliyon* **5**, e02095. doi:10.1016/j.heliyon.2019.e02095

Huang, J. L., Pourhosseinzadeh, M. S., Lee, S., Kramer, N., Guillen, J. V., Cinque, N. H., Aniceto, P., Momen, A. T., Koike, S. and Huising, M. O. (2024). Paracrine signalling by pancreatic delta cells determines the glycaemic set point in mice. *Nat. Metab.* **6**, 61-77. doi:10.1038/s42255-023-00944-2

Iwai, S. and Uyeda, T. Q. (2008). Visualizing myosin-actin interaction with a genetically-encoded fluorescent strain sensor. *Proc. Natl. Acad. Sci. USA* **105**, 16882-16887. doi:10.1073/pnas.0805513105

Jaiswal, A., Hoerth, C. H., Zuniga Pereira, A. M. and Lorenz, H. (2019). Improved spatial resolution by induced live cell and organelle swelling in hypotonic solutions. *Sci. Rep.* **9**, 12911. doi:10.1038/s41598-019-49408-2

Jing Liu, I.-H. C., Yi, C. and Joseph, I. (2014). Second harmonic super-resolution microscopy for quantification of mRNA at single copy sensitivity. *ACS Nano* **8**, 12418-12427. doi:10.1021/nn505096t

Kasprzak, A. A. (2007). The use of FRET in the analysis of motor protein structure. *Methods Mol. Biol.* **392**, 183-197. doi:10.1007/978-1-59745-490-2_13

Kim, K. Y., Kovacs, M., Kawamoto, S., Sellers, J. R. and Adelstein, R. S. (2005). Disease-associated mutations and alternative splicing alter the enzymatic and motile activity of nonmuscle myosins II-B and II-C. *J. Biol. Chem.* **280**, 22769-22775. doi:10.1074/jbc.M503488200

Kovacs, M., Toth, J., Hetenyi, C., Malnasi-Csizmadia, A. and Sellers, J. R. (2004). Mechanism of blebbistatin inhibition of myosin II. *J. Biol. Chem.* **279**, 35557-35563. doi:10.1074/jbc.M405319200

Krieg, M., Dunn, A. R. and Goodman, M. B. (2014). Mechanical control of the sense of touch by beta-spectrin. *Nat. Cell Biol.* **16**, 224-233. doi:10.1038/ncb2915

Kumar, A., Ouyang, M., Van den Dries, K., McGhee, E. J., Tanaka, K., Anderson, M. D., Groisman, A., Goult, B. T., Anderson, K. I. and Schwartz, M. A. (2016). Talin tension sensor reveals novel features of focal adhesion force transmission and mechanosensitivity. *J. Cell Biol.* **213**, 371-383. doi:10.1083/jcb.201510012

LaCroix, A. S., Lynch, A. D., Berginski, M. E. and Hoffman, B. D. (2018). Tunable molecular tension sensors reveal extension-based control of vinculin loading. *Elife* **7**, e33927. doi:10.7554/eLife.33927

Lagendijk, A. K., Gomez, G. A., Baek, S., Hesselson, D., Hughes, W. E., Paterson, S., Conway, D. E., Belting, H. G., Affolter, M., Smith, K. A. et al. (2017). Live imaging molecular changes in junctional tension upon VE-cadherin in zebrafish. *Nat. Commun.* **8**, 1402. doi:10.1038/s41467-017-01325-6

Lucas-Lopez, C., Allingham, J. S., Lebl, T., Lawson, C. P., Brenk, R., Sellers, J. R., Rayment, I. and Westwood, N. J. (2008). The small molecule tool (S)-(-)-blebbistatin: novel insights of relevance to myosin inhibitor design. *Org. Biomol. Chem.* **6**, 2076-2084. doi:10.1039/b801223g

Ma, X. and Adelstein, R. S. (2014). The role of vertebrate nonmuscle Myosin II in development and human disease. *Bioarchitecture* **4**, 88-102. doi:10.4161/bioa.29766

Ma, X., Kovacs, M., Conti, M. A., Wang, A., Zhang, Y., Sellers, J. R. and Adelstein, R. S. (2012). Nonmuscle myosin II exerts tension but does not translocate actin in vertebrate cytokinesis. *Proc. Natl. Acad. Sci. USA* **109**, 4509-4514. doi:10.1073/pnas.1116268109

Meng, F. and Sachs, F. (2011). Visualizing dynamic cytoplasmic forces with a compliance-matched FRET sensor. *J. Cell Sci.* **124**, 261. doi:10.1242/jcs.071928

Meng, F. and Sachs, F. (2012). Orientation-based FRET sensor for real-time imaging of cellular forces. *J. Cell Sci.* **125**, 743. doi:10.1242/jcs.093104

Meng, F., Suchyna, T. M. and Sachs, F. (2008). A fluorescence energy transfer-based mechanical stress sensor for specific proteins in situ. *FEBS J.* **275**, 3072-3087. doi:10.1111/j.1742-4658.2008.06461.x

Milberg, O., Shitara, A., Ebrahim, S., Masedunskas, A., Tora, M., Tran, D. T., Chen, Y., Conti, M. A., Adelstein, R. S., Ten Hagen, K. G. et al. (2017). Concerted actions of distinct nonmuscle myosin II isoforms drive intracellular membrane remodeling in live animals. *J. Cell Biol.* **216**, 1925-1936. doi:10.1083/jcb.201612126

Morimatsu, M., Mekhdjian, A. H., Adhikari, A. S. and Dunn, A. R. (2013). Molecular tension sensors report forces generated by single integrin molecules in living cells. *Nano Lett.* **13**, 3985-3989. doi:10.1021/nl4005145

Munnich, S., Pathan-Chhatbar, S. and Manstein, D. J. (2014). Crystal structure of the rigor-like human non-muscle myosin-2 motor domain. *FEBS Lett.* **588**, 4754-4760. doi:10.1016/j.febslet.2014.11.007

Muretta, J. M., Rohde, J. A., Johnsrud, D. O., Cornea, S. and Thomas, D. D. (2015). Direct real-time detection of the structural and biochemical events in the myosin power stroke. *Proc. Natl. Acad. Sci. USA* **112**, 14272-14277. doi:10.1073/pnas.1514859112

Murrell, M., Oakes, P. W., Lenz, M. and Gardel, M. L. (2015). Forcing cells into shape: the mechanics of actomyosin contractility. *Nat. Rev. Mol. Cell Biol.* **16**, 486-498. doi:10.1038/nrm4012

Ng, M. R., Besser, A., Brugge, J. S. and Danuser, G. (2014). Mapping the dynamics of force transduction at cell-cell junctions of epithelial clusters. *Elife* **3**, e03282. doi:10.7554/eLife.03282

Nordenfelt, P., Elliott, H. L. and Springer, T. A. (2016). Coordinated integrin activation by actin-dependent force during T-cell migration. *Nat. Commun.* **7**, 13119. doi:10.1038/ncomms13119

O'Connor, D. V. O. P.,D. (1984). *Time-correlated Single Photon Counting*. London: Academic Press.

Phillips, C. L., Fu, D., Herring, L. E., Armao, D. and Snider, N. T. (2022). Calpain-mediated proteolysis of vimentin filaments is augmented in giant axonal neuropathy fibroblasts exposed to hypotonic stress. *Front. Cell Dev. Biol.* **10**, 1008542. doi:10.3389/fcell.2022.1008542

Polacheck, W. J. and Chen, C. S. (2016). Measuring cell-generated forces: a guide to the available tools. *Nat. Methods* **13**, 415-423. doi:10.1038/nmeth.3834

Price, A. J., Cost, A. L., Ungewiss, H., Waschke, J., Dunn, A. R. and Grashoff, C. (2018). Mechanical loading of desmosomes depends on the magnitude and orientation of external stress. *Nat. Commun.* **9**, 5284. doi:10.1038/s41467-018-07523-0

Ringer, P., Weissl, A., Cost, A. L., Freikamp, A., Sabass, B., Mehlich, A., Tramier, M., Rief, M. and Grashoff, C. (2017). Multiplexing molecular tension sensors reveals piconewton force gradient across talin-1. *Nat. Methods* **14**, 1090-1096. doi:10.1038/nmeth.4431

Rothenberg, K. E., Scott, D. W., Christoforou, N. and Hoffman, B. D. (2018). Vinculin force-sensitive dynamics at focal adhesions enable effective directed cell migration. *Biophys. J.* **114**, 1680-1694. doi:10.1016/j.bpj.2018.02.019

Saitoh, M., Ishikawa, T., Matsushima, S., Naka, M. and Hidaka, H. (1987). Selective inhibition of catalytic activity of smooth muscle myosin light chain kinase. *J. Biol. Chem.* **262**, 7796-7801. doi:10.1016/S0021-9258(18)47638-7

Sellers, J. R. (2000). Myosins: a diverse superfamily. *Biochim. Biophys. Acta* **1496**, 3-22. doi:10.1016/S0167-4889(00)00005-7

Sellers, J. R. and Knight, P. J. (2007). Folding and regulation in myosins II and V. *J. Muscle Res. Cell Motil.* **28**, 363-370. doi:10.1007/s10974-008-9134-0

Sellers, J. R., Pato, M. D. and Adelstein, R. S. (1981). Reversible phosphorylation of smooth muscle myosin, heavy meromyosin, and platelet myosin. *J. Biol. Chem.* **256**, 13137-13142. doi:10.1016/S0021-9258(18)43018-9

Shih, W. M., Gryczynski, Z., Lakowicz, J. R. and Spudich, J. A. (2000). A FRET-based sensor reveals large ATP hydrolysis-induced conformational changes and three distinct states of the molecular motor myosin. *Cell* **102**, 683-694. doi:10.1016/S0092-8674(00)00090-8

Shoyer, T. C., Collins, K. L., Ham, T. R., Blanchard, A. T., Malavade, J. N., Johns, B. A., West, J. L. and Hoffman, B. D. (2024). Detection of fluorescent protein mechanical switching in cellulo. *Cell Rep. Methods* **4**, 100815. doi:10.1016/j.crmeth.2024.100815

Shutova, M. S., Spessott, W. A., Giraudo, C. G. and Svitkina, T. (2014). Endogenous species of mammalian nonmuscle myosin IIA and IIB include activated monomers and heteropolymers. *Curr. Biol.* **24**, 1958-1968. doi:10.1016/j.cub.2014.07.070

Spudich, J. A. (2001). The myosin swinging cross-bridge model. *Nat. Rev. Mol. Cell Biol.* **2**, 387-392. doi:10.1038/35073086

Sugita, S., Adachi, T., Ueki, Y. and Sato, M. (2011). A novel method for measuring tension generated in stress fibers by applying external forces. *Biophys. J.* **101**, 53-60. doi:10.1016/j.bpj.2011.05.046

Takanaga, H. and Frommer, W. B. (2010). Facilitative plasma membrane transporters function during ER transit. *FASEB J.* **24**, 2849-2858. doi:10.1096/fj.09-146472

Tullio, A. N., Bridgman, P. C., Tresser, N. J., Chan, C. C., Conti, M. A., Adelstein, R. S. and Hara, Y. (2001). Structural abnormalities develop in the brain after ablation of the gene encoding nonmuscle myosin II-B heavy chain. *J. Comp. Neurol.* **433**, 62-74. doi:10.1002/cne.1125

Vicente-Manzanares, M., Ma, X., Adelstein, R. S. and Horwitz, A. R. (2009). Non-muscle myosin II takes centre stage in cell adhesion and migration. *Nat. Rev. Mol. Cell Biol.* **10**, 778-790. doi:10.1038/nrm2786

Vicente-Manzanares, M., Newell-Litwa, K., Bachir, A. I., Whitmore, L. A. and Horwitz, A. R. (2011). Myosin IIA/IIB restrict adhesive and protrusive signaling to generate front-back polarity in migrating cells. *J. Cell Biol.* **193**, 381-396. doi:10.1083/jcb.201012159

Vidi, P. A., Liu, J., Salles, D., Jayaraman, S., Dorfman, G., Gray, M., Abad, P., Moghe, P. V., Irudayaraj, J. M., Wiesmuller, L. et al. (2014). NuMA promotes homologous recombination repair by regulating the accumulation of the ISWI ATPase SNF2h at DNA breaks. *Nucleic Acids Res.* **42**, 6365-6379. doi:10.1093/nar/gku296

Wei, Q. and Adelstein, R. S. (2000). Conditional expression of a truncated fragment of nonmuscle myosin II-A alters cell shape but not cytokinesis in HeLa cells. *Mol. Biol. Cell* **11**, 3617-3627. doi:10.1091/mbc.11.10.3617

Yamashita, S., Tsuboi, T., Ishinabe, N., Kitaguchi, T. and Michiue, T. (2016). Wide and high resolution tension measurement using FRET in embryo. *Sci. Rep.* **6**, 28535. doi:10.1038/srep28535

Zeng, W., Seward, H. E., Malnasi-Csizmadia, A., Wakelin, S., Woolley, R. J., Cheema, G. S., Basran, J., Patel, T. R., Rowe, A. J. and Bagshaw, C. R. (2006). Resonance energy transfer between green fluorescent protein variants: complexities revealed with myosin fusion proteins. *Biochemistry* **45**, 10482-10491. doi:10.1021/bi060943u